Ignition and high gain with ultrapowerful lasers*

Max Tabak,† James Hammer, Michael E. Glinsky, William L. Kruer, Scott C. Wilks, John Woodworth, E. Michael Campbell, and Michael D. Perry
Lawrence Livermore National Laboratory, Livermore, California 94550

Rodney J. Mason
Los Alamos National Laboratory, Los Alamos, New Mexico 87545

(Received 5 November 1993; accepted 12 January 1994)

Ultrahigh intensity lasers can potentially be used in conjunction with conventional fusion lasers to ignite inertial confinement fusion (ICF) capsules with a total energy of a few tens of kilojoules of laser light, and can possibly lead to high gain with as little as 100 kJ. A scheme is proposed with three phases. First, a capsule is imploded as in the conventional approach to inertial fusion to assemble a high-density fuel configuration. Second, a hole is bored through the capsule corona composed of ablated material, as the critical density is pushed close to the high-density core of the capsule by the ponderomotive force associated with high-intensity laser light. Finally, the fuel is ignited by suprathermal electrons, produced in the high-intensity laser–plasma interactions, which then propagate from critical density to this high-density core. This new scheme also drastically reduces the difficulty of the implosion, and thereby allows lower quality fabrication and less stringent beam quality and symmetry requirements from the implosion driver. The difficulty of the fusion scheme is transferred to the technological difficulty of producing the ultrahigh-intensity laser and of transporting this energy to the fuel.

I. INTRODUCTION

The plan of the paper is as follows. We first discuss and compare the gain model that describes the conventional approach to inertial fusion with the model that describes our proposed scheme. A discussion of the symmetry and stability properties of the new scheme follows. Next, we address how the laser intensity is to be determined. Then comes a description of the hole-boring scheme. We show a preliminary calculation integrating the various pieces of the scheme at the preignition scale. We also briefly describe the laser technology that makes this approach possible. Finally, we summarize the work and suggest some critical experiments.

II. GAIN MODELS

The isobaric gain model of Meyer-ter-Vehn[1,2] describes the conventional approach to inertial fusion. In this model, the fuel assembled by the implosion is composed of two parts: a relatively low-density and high-temperature hot spot, surrounded by a high-density low-temperature main fuel. The two are in pressure equilibrium. The central hot spot can equilibrate with the high-density region in contact with it, because during the stagnation process the sound speed in the gas is much greater than the shell closure velocity. The main fuel is about 1 sound-crossing time thick during the final stagnation when the shell moves to its converged radius from twice that radius. If a method can be found to deliver the ignition energy sufficiently rapidly (as is suggested in the present scheme), the gain can be calculated with the isochoric (uniform density) model of Kidder,[3] where the hot spot and main fuel are out of pressure equilibrium. The isochoric model compresses significantly more mass to much lower peak density. Therefore, by burning that extra mass its yield and gain are significantly larger than that of the isobaric model.

Fuel ignition requires that the hot spot reaches an average temperature of 5 keV within a fuel areal density of about 0.3–0.4 gm/cm^2, corresponding to an α particle range. The mass of the heated deuterium–tritium mixture (DT), M (g), is $4\pi(\rho_{\rm HS}r)^3/3\ \rho_{\rm HS}^2$. The internal energy of this fuel is then $E_{\rm HS}({\rm MJ})=575M({\rm g})$. The energy of the main fuel is dominated by the compressional energy: $E_M({\rm MJ})=0.35\alpha\rho_M^{2/3}M$, where α is the factor by which the cold fuel is nondegenerate: $P_M=2.3\times10^{12}\alpha\rho_M^{5/3}$ dyn/cm^2. In optimized systems $E_M \gg E_{\rm HS}$, although in realistic systems they are comparable. The thermonuclear yield is $Y\simeq QM\rho r/(\rho r+7)$, where $Q=334$ GJ/g and ρr is the total areal density. The burn efficiency can be approximated as $\frac{1}{2}(\rho r/7)^{1/2}$. The gain, $G\propto(\rho r)^{1/2}/\rho_M^{2/3}$.

If there is no hot spot, $\rho r\propto E^{1/3}\rho^{4/9}$, $G\propto E^{1/6}\rho^{-4/9}$, and the gain is optimized at zero density. Unfortunately, the hot spot would require infinite input energy at zero density. Therefore, the optimum hot spot densities are different from zero and depend on the relationship between the hot spot and the main fuel. The isobaric constraint implies $\rho_M\propto(T_{\rm HS}\rho_{\rm HS}/\alpha)^{0.6}$, where $T_{\rm HS}$ is the hot spot temperature measured in keV. The total energy in MJ in the compressed system in the isobaric model is $E_{M-T-V}=5.8\times10^6T_{\rm HS}^3/(\alpha^2\rho_M^{10/3})+0.35\alpha M\rho_M^{2/3}$. If the hot spot and main fuel are not in pressure equilibrium, as is the case when the ignition energy is injected sufficiently rapidly, the gain may be calculated in the isochoric (uniform density) model of Kidder.[3] The total energy in the compressed system in MJ in this model is $E_K=0.031\ T_{\rm HS}/\rho^2+0.35\alpha M\rho^{2/3}$. If the gain is maximized for fixed energy coupled to the compressed core,

*Paper 6I2, Bull. Am. Phys. Soc. 38, 2010 (1993).
†Invited speaker.

 1070-664X/94/1(5)/1626/9/$6.00

TABLE I. Comparison of optimal quantities in the isobaric and isochoric models as functions of the internal energy of the initial system (ηE) in MJ.

Property	Isobaric model	Isochoric
Gain	$1.5 \times 10^3 \eta(\eta E)^{0.3}$	$3 \times 10^4 \eta(\eta E)^{0.4}$
$R_{\text{hot spot}}(\mu\text{m})$	$190(\eta E)^{0.5}$	$120(\eta E)^{0.5}$
$R_{\text{main fuel}}(\mu\text{m})$	$280(\eta E)^{0.5}$	$1200(\eta E)^{0.6}$
$\rho_{\text{main fuel}}(\text{g/cm}^3)$	$358(\eta E)^{-0.3}$	$33(\eta E)^{-0.5}$
$\text{Pr}_{\text{stag}}(\text{Mbar})$	$8.4\times 10^4(\eta E)^{-0.5}$	$780(\eta E)^{-0.8}$
Mass (mg)	$23(\eta E)^{1.2}$	$230(\eta E)^{1.3}$

$$G_{M-t-V}=6\times 10^3\eta(\eta E/\alpha^3)^{0.3}$$

and

$$G_K=3\times 10^4\eta(\eta E/\alpha^3)^{0.4},$$

where η is the coupling efficiency and E is the incident driver energy.

In the directly driven implosions of the conventional fusion scheme, α is required to be 2 or greater, so that the Rayleigh–Taylor instability during the implosion is sufficiently stabilized by ablation stabilization that the capsule survives the implosion. The Takabe[4] formula gives the Rayleigh–Taylor growth rate: $\gamma_{\text{RT}}=0.9(gk)^{0.5}-3v_A k$, where g is the acceleration, k is the wave number of the perturbation mode and v_A is the ablation velocity. The ablation velocity is given by the mass ablation rate divided by the shell density. Decreasing the ablator and fuel densities by increasing α, increases the ablation velocity, and thereby the shell stability. In addition, the decreased shell density produces a thicker shell and less feedthrough of the perturbation to the hot spot–main fuel interface.

In order to tie these simple models more closely to more detailed calculations, we take the hot spot radius at three times the value required for maximum gain in the isobaric model. This is done for two reasons. First, in order to ensure robust ignition, capsules are overdriven so that they ignite while still imploding at a radius larger than that required to obtain maximum gain. Second, the hot spot radius is tripled so that the convergence ratio (CR) of initial ablator radius to converged hot spot radius is less than 50 for megajoule scale lasers. Increasing the hot spot radius by a factor of 3 reduces the gain by a factor of 2. Therefore, the gain in the isobaric model is given by $G_{M-t-V}=1.5\times 10^3\eta(\eta E)^{0.3}$. Table I shows the gain, column density, density, fuel mass, hot spot and main fuel radii, and stagnation pressure in the two models. The isochoric model compresses significantly more mass to much lower peak density. In addition, the stagnation pressure in the isochoric model is almost two orders of magnitude lower than that in the isobaric. This great reduction in concentration of energy eases the required implosion quality.

The hydrodynamic efficiency, η, CR, and in-flight-aspect ratio (IFAR) are calculated in a model of Rosen and Lindl,[5] based on work by Max, McKee, and Mead.[6] The model assumes that the energy is completely absorbed at the critical surface. We study the case where S, the ratio of the critical radius to the ablation radius, is 1.3. This misses the effect of distributed absorption due to inverse bremsstrahlung and the intensity dependence of S in the model of Max *et al.*[6] However, the point of this analysis is to compare the isobaric and isochoric models of gain using the same implosion model. In fact, the peak hydrodynamic efficiencies of 8% and the maximum gain for input energy of 10 MJ (about 100) calculated for the isobaric model are consistent with much more detailed derivations.[7]

Our procedure is as follows. First, we calculate the required implosion velocity to supply the specific energy of the compressed core:

$$v_{\text{imp}}=(2\eta E/M)^{1/2}.$$

The rocket exhaust velocity is then given by

$$v_{\text{exh}}=4.6\times 10^7 I^{0.33}\lambda^{0.7}(\text{cm/s}),$$

where I is the intensity in 10^{14} W/cm^2, and λ is the laser wavelength in microns. We used $\frac{1}{3}\,\mu$m light. The areal mass ablation rate, $\dot{m}$, is

$$\dot{m}=1.8\times 10^5 I^{1/3}\lambda^{-4/3}(\text{g/cm}^2\,\text{s}).$$

The hydrodynamic efficiency for constant intensity, η, is given by

$$\eta=0.7\,\dot{m}\,v_{\text{imp}}{}^2/(2I)x/(1-x),$$

where the rocket equation, $\log(x)=v_{\text{imp}}/v_{\text{exh}}$, has been used. The factor 0.7 takes into account that as the capsule implodes and the critical density recedes, only 70% of the light will hit the target. The initial shell radius, R, is determined in a thin shell model by assuming that the payload reaches v_{imp} after accelerating half of its initial radius. Integrating the rocket equation in time relates R to the fraction of mass ablated. The shell density, ρ, is obtained from the equation of state, $P=2.3\alpha\rho^{5/3}$ (Mbar). The ablation pressure is given by $\dot{m}\,v_{\text{exh}}$. Because we know the required payload mass and the fraction of the initial mass ablated, we can calculate the initial shell mass. Given the shell density at this time, we obtain its thickness, and hence the IFAR. Similarly, we know the converged main fuel and hot spot radii and can therefore obtain the CR. For the isobaric model, the CR is calculated to the outside of the hot spot, while for the isochoric model we use the outside of the main fuel. This is reasonable because in our uniform density scheme we are not relying on the compression laser for ignition.

Figure 1 plots gain, IFAR, and CR versus compression laser energy for the two models for typical intensities. We chose to show $I=3\times 10^{13}$ W/cm^2 for the isochoric model, and $I=2\times 10^{14}$ W/cm^2 for the isobaric model. Because the isochoric model requires much lower specific energies and implosion velocities than does the isobaric model, it is better matched with low exhaust velocities and hence lower intensities. This choice of intensities produces approximately equal payload fractions, and therefore rocket efficiencies in the two models. This choice also corresponds to optimum tradeoffs among gain, CR, and IFAR over the bulk of the input energy range. The option of using lower intensity, may also reopen the possibility of using longer

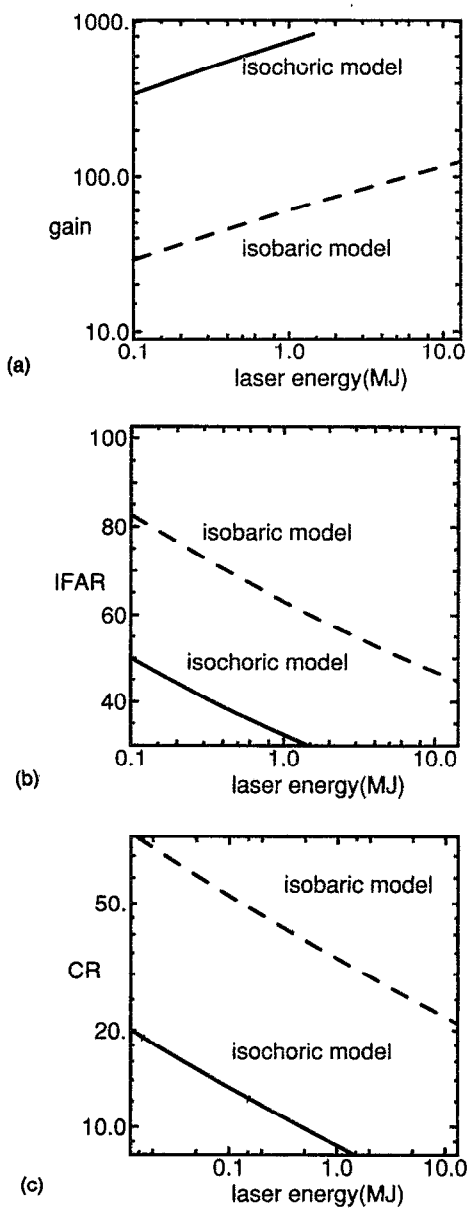

FIG. 1. (a) Gain; (b) in-flight-aspect-ratio; and (c) convergence ratio, all plotted versus input laser energy for isochoric (solid line) and isobaric (dashed line) models.

wavelength light ($\frac{1}{2}$ and 1 μm instead of $\frac{1}{3}$ and 1/4 μm). This could reduce the requirement for frequency conversion of Nd glass or more advanced solid state lasers with the attendant cost, complexity, and inefficiency.

III. FUEL ASSEMBLY

The much lower values of CR and IFAR associated with the isobaric model indicate that the fuel assembly should be much less sensitive to laser light nonuniformities and growth of hydrodynamic instabilities than the conventional ICF scheme. The fast ignition approach generates fewer Rayleigh–Taylor e-foldings during the implosion. The linear growth rate for electron-driven ablation, γ_{RT}, is given by

$$\gamma_{\mathrm{RT}} \approx 0.9(gk)^{1/2} - 3v_A k.$$

The number of e-foldings for the ablation front instability is the time integral of this:

$$\begin{aligned} N_{\mathrm{RT}} &\approx 0.9(gkt^2)^{1/2} - 3v_A kt \\ &= 0.9(kR)^{1/2} - 3\,\delta R\,k \\ &= 0.9l^{1/2} - 3(1-x)l/\mathrm{IFAR}, \end{aligned}$$

where the relation $k = l/R$ between wave number and spherical harmonic index is used. For the intensities used in the plots above, the stabilization factor, $(1-x)/\mathrm{IFAR}$, for the isochoric model was about twice that for the isobaric model.

Not only will the new scheme produce less Rayleigh–Taylor growth, but the importance of mix will also be reduced. Because the fast ignition scheme does not rely on a central hot spot for ignition, mix cannot quench ignition. Fast ignition has a different set of failure modes from conventional ICF. Hydrodynamic instabilities could, in principle, prevent the assembly of the fuel to the required density. However, core densities and areal densities greater than those needed for the fast ignitor have already been achieved in the laboratory. The Osaka group[8] has obtained compressed CDT densities around 600 gm/cm^3 and areal densities of about 0.6 g/cm^2. In these experiments, they imploded CDT shells driven with 9 kJ of 0.53 μm light incident and about 4 kJ absorbed. Only 10%–15% uniformity (5% RMS) in irradiation was obtained, even with random phase plates to smooth the laser beams. The peak intensity was $1\text{–}2\times10^{14}$ W/cm^2, and the convergence ratio was between 20 and 40. These data are shown in Fig. 2. The measured yield was reduced at least two orders of magnitude from that predicted for an unmixed implosion. These data show that implosions of insufficient quality to produce an adequate hot spot for the conventional ICF scheme are nevertheless good enough to produce compressed configurations suitable for ignition by exogenous heating after the implosion was completed.

IV. LASER SCALE REQUIREMENTS

What requirements are set on the ignition laser? The energy flow and ignition region disassembly times set the required ignition laser duration and intensity. The energy flow goes from laser light to suprathermal electrons to thermal electrons to fuel ions, and finally to the kinetic energy of the disassembling fuel. Each of these steps has a characteristic time: $\tau_{\gamma-e}$, the laser-electron time is approximately one laser cycle or 10^{-15} s. We estimate the other times for DT density of 300 g/cm^3 at a temperature of 5 keV: τ_{ee}, the suprathermal to thermal coupling time is less than 10^{-13} s, while τ_{ei}, the electron–ion coupling time, is about 10^{-12} s. We want to heat an α-particle range, ρR, to approximately 0.4 g/cm^2. This gives a fuel radius of 10 μm. The sound speed at 5 keV of about 1 μm/ps, yields τ_D, the disassembly time, of 10 ps. The laser duration at peak intensity should be between τ_{ei} and τ_D. If the laser duration is much less than τ_{ei}, the electrons will be heated and their

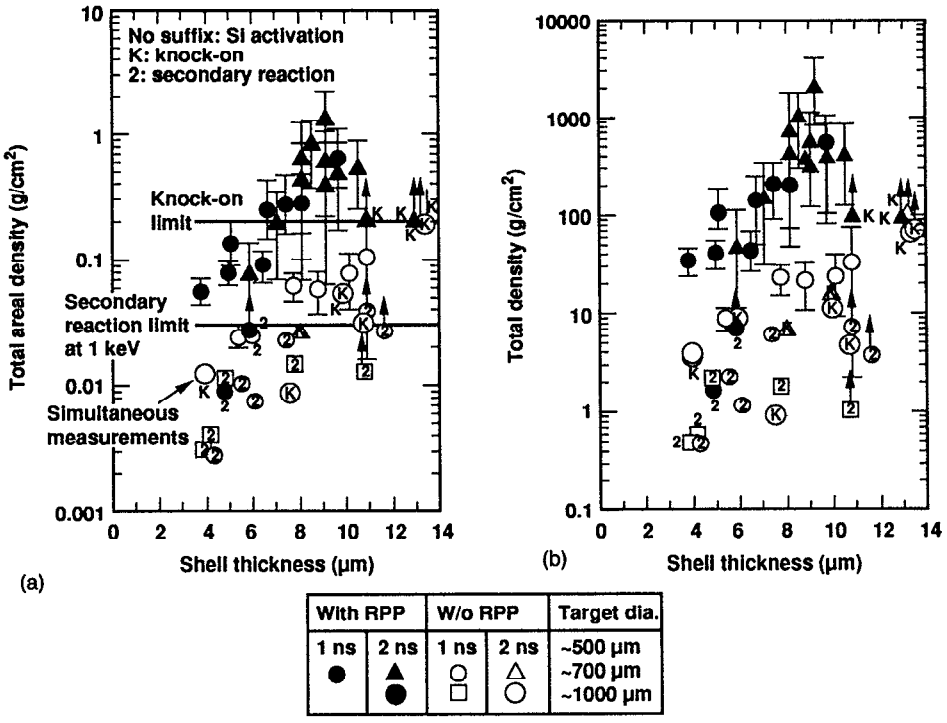

FIG. 2. (a) Areal density and (b) density versus shell thickness in imploded CDT shells (from Ref. 8).

pressure will disassemble the target before the ions are heated to fusion temperatures. If the fuel is ultimately heated to 10 keV by the laser, the energy supplied must be $3\times10^8/\rho^2 J$ or 3 kJ for this case. The power is $1.2\times10^{17}/\rho W$ or 4×10^{14} W. The intensity is 2×10^{17} $\rho W/\mathrm{cm}^2$ or 8×10^{19} $\mathrm{W/cm}^2$. These quantities describe what must be delivered to the fuel. Any coupling inefficiencies will increase the associated laser requirements.

The scale of the ignition laser is set by coupling efficiencies and the required ignition energy. Figure 3 shows the electron range as a function of electron energy in DT. Electrons with energies between 500 keV and 1 MeV have ranges comparable to a 3.5 MeV α-particle range. Figure 4 shows the suprathermal electron temperature as a function of $I\lambda^2$, where I is the intensity and λ is the laser wavelength. Shown in the figure are the results of particle-in-cell (PIC)[9] calculations, with s and p polarized light together with data obtained by bremsstrahlung measurements from irradiations 500–1000 ps long with 10.6 μm wavelength,[10] 600 fs long with 1.053 μm wavelength,[11] and 80 fs long with 0.8 μm wavelength.[12] The solid curve shows the ponderomotive potential. Laser irradiations with values of $I\lambda^2$ between 10^{19} W $\mu\mathrm{m}^2/\mathrm{cm}^2$ and 10^{20} W $\mu\mathrm{m}^2/\mathrm{cm}^2$ will produce electrons with path lengths less than 1 g/cm^2. Mul-

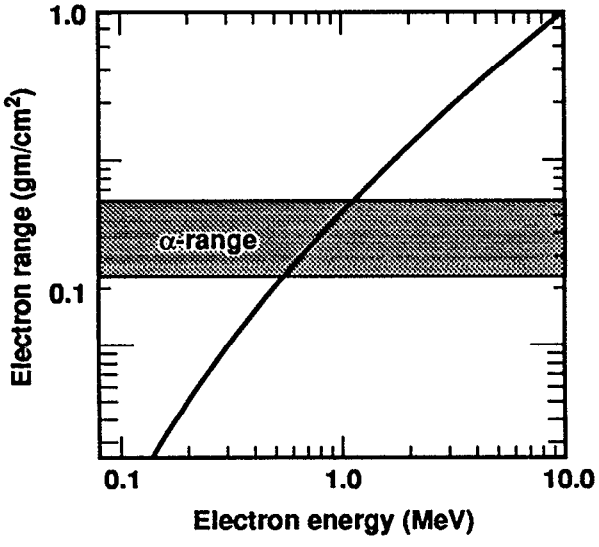

FIG. 3. Electron range versus electron kinetic energy in DT.

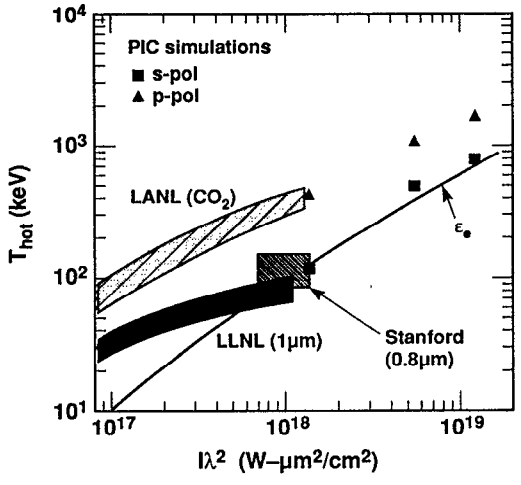

FIG. 4. Suprathermal electron temperature versus $I\lambda^2$.

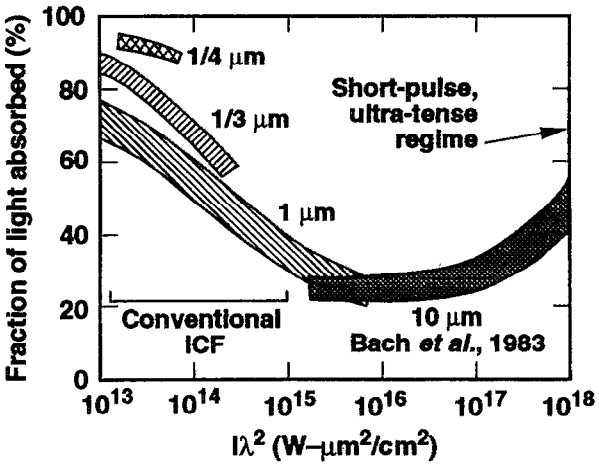

FIG. 5. Laser light absorption fraction versus $I\lambda^2$ for a variety of laser wavelengths.

tiple scattering and self-generated electric and magnetic fields (see below) may further reduce the region heated by these electrons.

We anticipate a regime of high absorption at very high intensity dominated by noncollisional mechanisms. Figure 5 shows the laser light absorption fraction as a function of $I\lambda^2$ for a variety of wavelengths.[13] The absorption at a particular $I\lambda^2$ varies more than shown, being a function of peak plasma density, plasma scale height, laser polarization, and angle of incidence. Individual high intensity CO_2 shots measured absorption as high as 65%–70%.[10] This high absorption is ascribed to new mechanisms: the so-called not-so-resonant resonant absorption of Brunel[14] and $j\times B$[15] heating, which turns on at high intensity when the electrons become relativistic, as well as resonant absorption. Additional absorption is also ascribed to the rippling of the critical surface.[10] The PIC code, ZOHAR,[16] was used to simulate these processes at $I\lambda^2=10^{19}$ W μm^2/cm^2. Over a wide variety of conditions absorptions in the range 30%–50% were obtained.[17]

V. HOLE BORING

The efficient transport of hot electrons to the fuel is a key issue. In our scheme, the fuel is first imploded to high density. This leaves a corona with critical density many hot spot diameters from the dense core. If we couple laser light to suprathermal electrons at this position, the coupling of the electrons to the core is expected to be very poor (the solid angle subtended by the hot spot will be much less than 1% of 4π sr). We need to bring the intense light much closer to the compressed core when its energy is transferred to the suprathermal electrons. This is possible because of two facts. First, because of relativistic effects,[18] critical density is increased by the relativistic factor, γ. Since

$$\omega_{pe}^2=4\pi n_e e^2/(\gamma m_e), \quad n_{cr}=n_{cr0}(1+I\lambda^2/10^{18})^{1/2}.$$

Second, we can push critical density by using the ponderomotive pressure. Momentum conservation gives this pressure as $2I/c$ for completely reflected light or I/c for completely absorbed light. This pressure is prodigious at the high intensities of interest. For $I=3\times10^{20}$ W/cm^2, I/c is 100 Gbars. Figure 6 shows a ZOHAR[16] calculation of a hole being bored through a plasma around the critical density, with $I\lambda^2=10^{19}$ W μm^2/cm^2. Its recession velocity was $1/40c$. We intend to bore holes through the hundreds of microns of corona by increasing the laser intensity from about 10^{17}–10^{19} W/cm^2, as the plasma density increases from critical density to 100 critical density so that the recession velocity is maintained near 1 μm/ps. This will require several hundreds of picoseconds of prepulse.

In recent experiments[19] with short pulse irradiations with intensity about 10^{16} W/cm^2, the Doppler shift of light

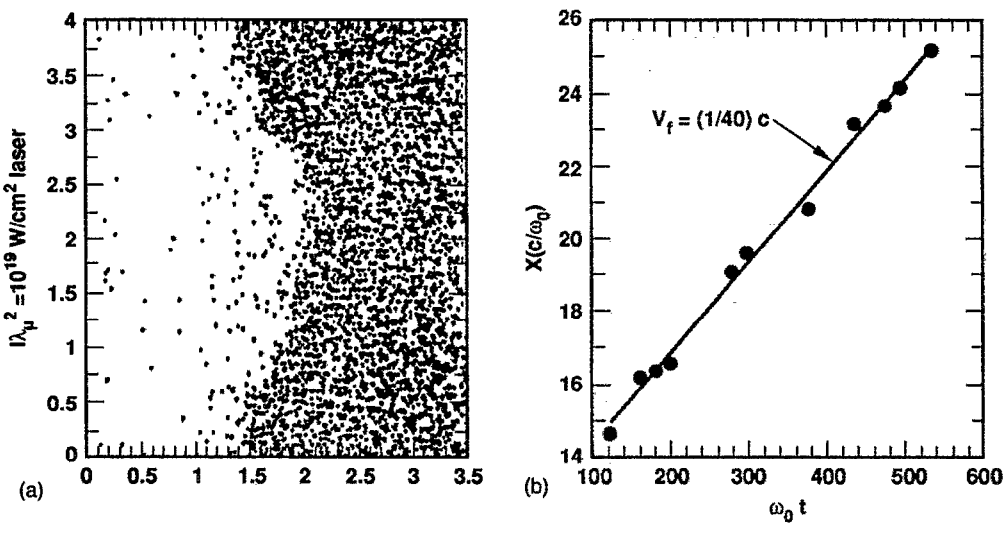

FIG. 6. (a) A snapshot of ion density from the PIC code (ZOHAR), showing dimpling due to ponderomotive force; and (b) the position of the critical surface ($\lambda/2\pi$) versus the laser cycle. The slope is $1/40c$.

reflected from the critical surface was measured. The ponderomotive force had to be included in the theoretical model to explain the reduction of the measured blue shift. In experiments driven with 500–1000 ps CO_2[20] laser pulses at $I=10^{16}$ W/cm^2, harmonics up to the 46th were observed with a flat spectrum. This was explained in a model[21] in which the electron density profile was steepened with an upper shelf density at least 2000 times the critical density, with the lower shelf at one-tenth of critical density. The ponderomotive force was invoked to explain this steepening. Less dramatic steepening has been interferometrically measured[22] in 30 ps exposures of 1.06 μm light at 3×10^{14} W/cm^2. Inhibited electron transport from critical density inward can also contribute to a density jump near critical density.[6]

The current available data demonstrate the existence of the ponderomotive force, but not directly the hole boring required by this concept. We are beginning an experimental program to study this effect. Of particular concern is filamentation and defocusing of the incident laser beam. PIC calculations, in which both a critical surface and a long underdense plasma exist show filamentation in the underdense plasma, as the light reflected from the critical surface interferes with the incident light. PIC simulations[9] and analytic models[23] show a Rayleigh–Taylor-like instability at the plasma–light interface at critical density, with a growth time of tens of femtoseconds. The PIC simulation showed the saturated state of this instability as a bubble empty of plasma through which the light propagated surrounded by plasma walls. These simulations are approximately ten microns in extent, not the hundreds of microns of interest for this application. Ray trace calculations show that filamentation and beam flicker do occur, but over long times the laser path is depleted of plasma and the beams can propagate without significant refraction. Even if this occurs, stimulated scattering may still be a concern[24] until the electron thermal velocity in the channel becomes comparable to the oscillatory velocity. All of the calculations to this time have been two dimensional. Three-dimensional effects could be significant.

VI. SUPRATHERMAL TRANSPORT AND AN INTEGRATED PREIGNITION CALCULATION

Once the optical channel has been bored through the plasma, the suprathermal electrons produced at critical density must propagate to the high-density core. The transport of these electrons will be significantly modified by the self-consistent macroscopic electric and magnetic fields that their flow establishes. Electric potentials comparable to the suprathermal electron temperatures are established to maintain approximate neutrality. Transport into the overdense plasma should be inhibited initially, because the conductivity of the plasma is not high enough to allow an adequate return current. Transport into the underdense plasma should be inhibited because there are insufficient charge carriers to return the current. Because of finite spot size effects, the electric fields thus established should have nonvanishing curl and therefore establish magnetic fields.

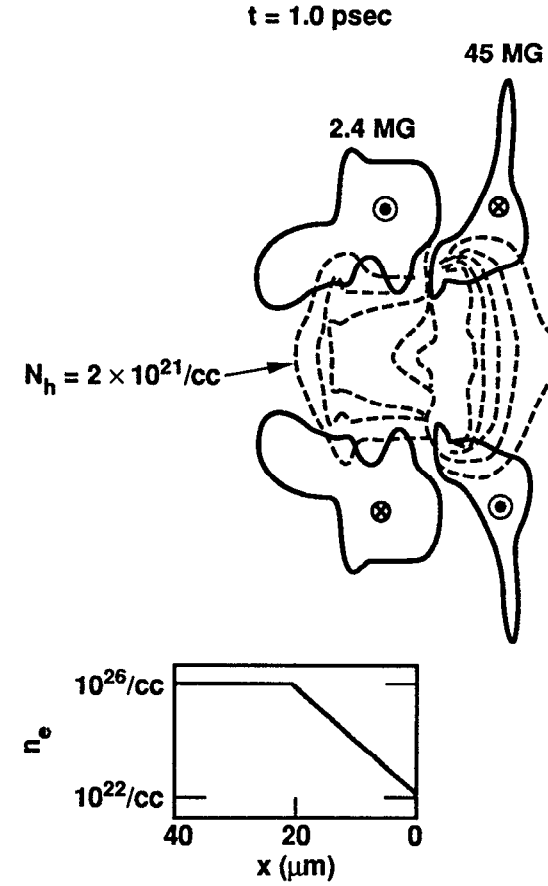

FIG. 7. Contour plots of magnetic field, B_z, and suprathermal density, n_h. The solid contours are for values of the magnetic field shown. The dashed contours are of the suprathermal density (contour interval 2×10^{21}/cm^3). The initial electron density profile is shown below the first set of contour plots; it is uniform in the y direction. The laser light is incident from the right with a beam diameter of 20 μm. At 1 ps, the maximum values of the magnetic field are 5 and 200 MG in the bulk and surface, respectively; and the maximum value of the suprathermal density is 3×10^{22}/cm^3.

ZOHAR simulations[9] have shown magnetic fields of order 100 MG in a plasma a few times the critical density for irradiation at $I\lambda^2=10^{19}$ W μm^2/cm^2.

ANTHEM,[25,26] a two-dimensional (2-D) hydrodynamic code, which implicitly solves for the electric and magnetic fields, and does not assume quasineutrality, was used to study an example closer to the requirements of this ignition technique. Figure 7 shows the geometry and the main results. The plasma density ramps up from 10^{22}/cm^3 to 10^{26}/cm^3 in 20 μm, with the plateau extending for another 20 μm. Electrons with energy flux 10^{20} W/cm^2 and temperature of 1 MeV were injected into a zone with electron density 10^{22}/cm^3. In 1 psec, magnetic fields of 5 MG were obtained in the overdense region, while in the underdense region they reach 200 MG. The electrons are collimated by the magnetic fields, more at 1 ps than at 100 fs.

A series of calculations using the computer code LASNEX[27] at the preignition scale are used to illustrate the fast ignitor process. First, a capsule is directly imploded with 550 J of 527 nm light radially incident. The fuel in the

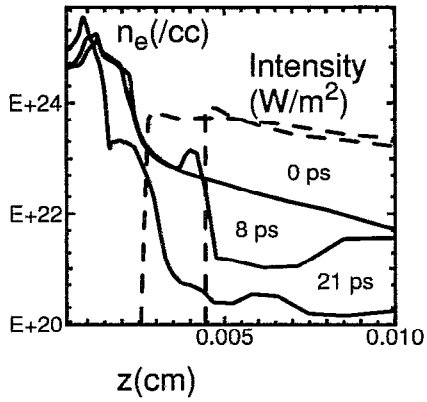

FIG. 8. Electron density (cm^3) and laser intensity (W/m^2) at three times along the symmetry axis in a hole-boring calculation. The $\frac{1}{4}$ μm light is incident from the right.

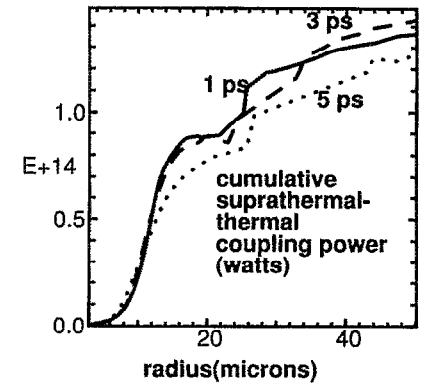

FIG. 10. Snapshots of the cumulative power (10^{14} W) coupling from suprathermal electrons to thermal electrons as one integrates outward from the center of the capsule.

capsule is originally cryogenic DT. Then 20 ps before peak compression, a $\frac{1}{4}$ μm laser with power 1–1.5$\times 10^{14}$ W is focused at $f/10$ with a Gaussian beam profile upon the corona remaining after the implosion. The peak intensity was about 10^{20} W/cm^2. Figure 8 demonstrates the hole-boring process by showing the electron density on the symmetry axis at this and two later times, together with the light intensity also on axis at the two later times. Critical density has been pushed 40 μm during this period. Figure 9 shows isocontours of electron density and laser intensity at this final time, 21 ps after the hole-boring started. The isocontours of density accumulate near the laser focal spot demonstrating the plasma steepening. The critical density surface is clearly very distorted. Other hole boring calculations have used lower powers and intensities for longer times. We have not yet optimized the laser pulse shapes used in this process.

The density on the symmetry axis of the hole-boring calculation was used as the density profile of a spherically symmetric one-dimensional (1-D) burn calculation. Our thermonuclear burn code does not accurately treat suprathermal electron transport in two dimensions (2D), so we made a 1-D approximation, where transport is more accurately treated.[28] We intend, in the future, to couple 2-D information from ANTHEM simulations to our burn code. The suprathermal electrons are transported in a multigroup approximation with self-consistent electric fields, so that quasineutrality is maintained. At the preignition scale we expect the suprathermal electrons to burn through the target, so a 1-D treatment should be reasonable. Electrons with temperature 300 keV were injected into a zone centered at a radius of 22 μm. Figure 10 shows that the bulk of the suprathermal–thermal coupling takes place in the high-density region, where collision rates between hot and cold electrons and between cold electrons and ions are highest. Figure 11 shows that we can raise the ion temperature to between 3 and 10 keV with the suprathermal heating. In this example, the thermal electrons and ions are not well coupled, because the plasma density is too low. Nevertheless, these ion temperatures are adequate to obtain significant thermonuclear burn. Figure 12 shows the source energy, thermonuclear yield, the collisional coupling between suprathermal and thermal electrons, the coupling between suprathermals and thermals via collective fields, and the amount of energy resident in the suprathermal electrons. The energy remaining in suprather-

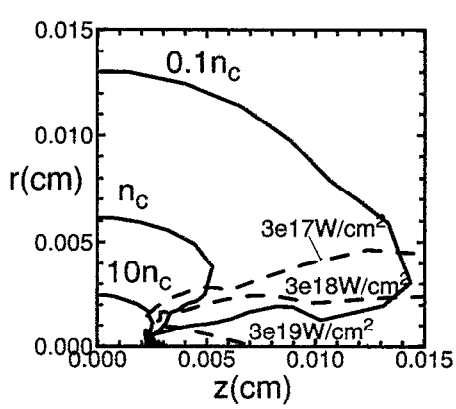

FIG. 9. Isocontours of laser intensity and electron density (multiples of critical density) 21 ps after the start of the hole-boring calculation.

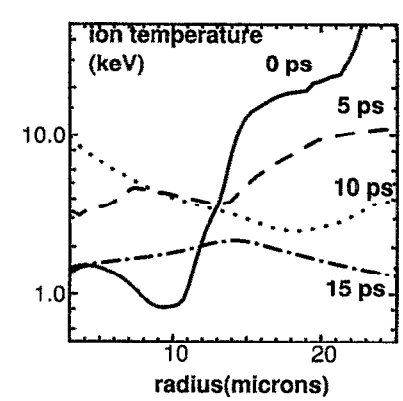

FIG. 11. Snapshots (t=0, t=5 ps, t=10 ps, and t=15 ps) of ion temperature in the capsule described above as it is heated by the suprathermal electrons.

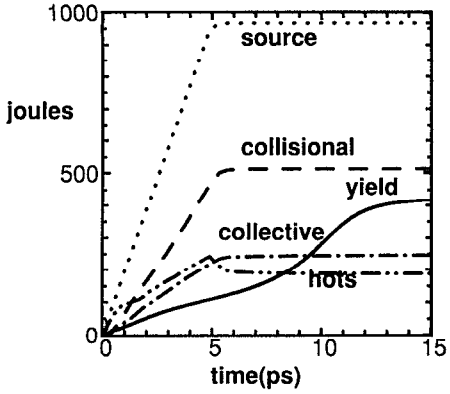

FIG. 12. Time histories of suprathermal source energy, coupling via collective fields, the total energy resident in the suprathermal electrons, collisional coupling between the suprathermal and thermal electrons, and thermonuclear yield.

mals corresponds to electrons that have escaped into the underdense plasma. The large fraction of energy coupled via collective $j \cdot E$ heating showed that suprathermal transport was significantly inhibited. The total energy supplied in this series of calculations was about 5.2 and 0.4 kJ of thermonuclear yield was produced.

VII. LASER PROSPECTS AND PROOF-OF-PRINCIPLE

The Petawatt laser,[29] due to be completed in the fall of 1995, will provide an opportunity for proof-of-principle experiments. The goal of the Petawatt project is to produce 1.0 kJ of 1.053 μm light in a twice diffraction limited beam, with pulse length variable between 0.5 and 20 ps. Peak intensity greater than 10^{21} W/cm^2 is possible. The technique to accomplish this is chirped pulse amplification[30] using a modified Nova beamline with the final amplifiers removed. Among the many innovations that make this project possible is the development of dielectric diffraction gratings that are used to compress the beam. This technology has been demonstrated with a damage threshold of over 1 J/cm^2 with some possibility of going to 6 J/cm^2 for nanosecond pulses. In addition, the size of the gratings can be increased to the meter scale from the current 30 cm. Hence, short pulse lasers with energies substantially larger than the Petawatt may become feasible.

The Petawatt laser will be able to bore holes through plasmas in situations where the oscillatory velocity of electrons in the laser beam is much larger than the thermal velocity; that is, where the ponderomotive pressure dominates the hole boring. There is sufficient energy to push critical density about 100 μm. The laser will use the Nova ten-beam target area, so the other nine Nova beams will be available to preimplode a CDT shell. The Petawatt laser will be synchronized to the remaining Nova beams to within 10 ps. Our goal is to raise the temperature of this preimploded shell 500–1000 eV and produce 10^{11} neutrons, many orders of magnitude more than would be expected without the suprathermal heating.

VIII. SUMMARY

The Fast Ignitor concept is a very speculative approach to inertial fusion, which offers the possibility of producing significantly higher gains with much less driver energy than the conventional approach. It employs three phases: first, a capsule is imploded to form a high-density core; second, a hole is drilled through the coronal plasma with a ponderomotive force; finally, the core is ignited with suprathermal electrons generated by the ignition laser at high $I\lambda^2$. It shifts the technical risk from the symmetry and stability issues of the conventional approach to the relatively unexplored issues of coupling and transport at high intensity and the laser technology required to produce those intense, short pulses.

If the project succeeds it could have significant impact on the practicality of inertial fusion: driver energy scales could be reduced, and target fabrication finish and irradiation symmetry requirements could be eased. The higher gain curves could support a reactor using a high repetition rate, small yield explosions or low repetition rate, high yield explosions. If successful, the fast ignitor concept would make some driver candidates currently considered unacceptable due to their low efficiency viable as a result of the higher gain achievable.

ACKNOWLEDGMENTS

The authors wish to thank Christopher Darrow, Dan Klem, Steve Lane, and Bruce Langdon for useful comments and discussions; and Mordecai Rosen and John Lindl for encouragement.

This work was performed under the auspices of the United States Department of Energy by the Lawrence Livermore National Laboratory under Contract No. W-7405-ENG-48.

[1] J. Meyer-ter-Vehn, Nucl. Fusion **22**, 561 (1982).

[2] See National Technical Information Service Document No. DE84017287/XAB (M. D. Rosen, J. D. Lindl, and A. R. Thiessen, "Simple models of high-gain targets—Comparisons and generalizations," in *Laser Program Annual Report-83*, UCRL-50021-83, pp. 3–5–3–9). Copies may be ordered from the National Technical Information Service, U.S. Department of Commerce, 5285 Port Royal Road, Springfield, Virginia 22161.

[3] R. Kidder, Nucl. Fusion **16**, 405 (1976).

[4] H. Takabe, L. Montierth, and R. L. Morse, Phys. Fluids **26**, 2299 (1983); H. Takabe, K. Mima, L. Montierth, and R. L. Morse, *ibid.* **28**, 3676 (1985); M. Tabak, D. H. Munro, and J. D. Lindl, Phys. Fluids B **2**, 1007 (1990).

[5] See National Technical Information Service Document No. DE84017287/XAB (M. D. Rosen and J. D. Lindl, "Model for gain vs laser energy in direct drive targets," in *Laser Program Annual Report-83*, UCRL-50021-83, pp. 3-9–3-13). Copies may be ordered from the National Technical Information Service, U.S. Department of Commerce, 5285 Port Royal Road, Springfield, Virginia 22161.

[6] C. E. Max, C. F. McKee, and W. C. Mead, Phys. Fluids **23**, 1620 (1980).

[7] C. P. Verdon, Bull. Am. Phys. Soc. **38**, 2010 (1993).

[8] H. Azechi, T. Jitsuno, T. Kanabe, M. Katayama, K. Mima, N. Miyanaga, M. Nakai, S. Nakai, H. Nakaishi, M. Nakatsuka, A. Nishiguchi, P. A. Norrays, Y. Setsuhara, M. Takagi, M. Yamanaka, and C. Yamanaka, Laser Part. Beams **9**, 2 (1991).

[9] S. C. Wilks, W. L. Kruer, M. Tabak, and A. B. Langdon, Phys. Rev. Lett. **69**, 1383 (1992).

[10] W. Priedhorsky, D. Lier, R. Day, and D. Gerke, Phys. Rev. Lett. **47**,

1661 (1981); D. R. Bach, D. E. Casperson, D. W. Forslund, S. J. Gitomer, P. D. Goldstone, A. Hauer, J. F. Kephart, J. M. Kindel, R. Kristal, G. A. Kyrala, K. B. Mitchell, D. B. van Hulsteyn, and A. H. Williams, *ibid.* **50**, 2082 (1983).
[11]D. Klem, Bull. Am. Phys. Soc. **37**, 1382 (1992).
[12]J. D. Kmetec, C. L. Gordon, III, J. J. Macklin, B. E. Lemoff, G. S. Brown, and S. E. Harris, Phys. Rev. Lett. **68**, 1527 (1992).
[13]E. M. Campbell (private communication, 1993).
[14]F. Brunel, Phys. Rev. Lett. **59**, 52 (1987).
[15]W. L. Kruer and K. Estabrook, Phys. Fluids **28**, 430 (1985).
[16]A. B. Langdon and B. F. Lasinski, in *Methods in Computational Physics*, edited by J. Killeen, R. Alder, S. Fernbach, and M. Rotenberg (Academic, New York, 1976), Vol. 16, p. 327.
[17]S. C. Wilks, Phys. Fluids B **5**, 2603 (1993).
[18]P. Kaw and J. Dawson, Phys. Fluids **13**, 472 (1970).
[19]X. Liu and D. Umstadter, Phys. Rev. Lett. **69**, 1935 (1992).
[20]R. L. Carman, D. W. Forslund, and J. M. Kindel, Phys. Rev. Lett. **46**, 29 (1981).
[21]B. Bezzerides, D. W. Forslund, and J. M. Kindel, Phys. Rev. Lett. **49**, 202 (1982).
[22]D. T. Atwood, D. W. Sweeney, J. M. Auerbach, and P. H. Y. Lee, Phys. Rev. Lett. **69**, 184 (1978).
[23]E. G. Gamaly, "The instability of the overdense plasma boundary induced by the action of the powerful photon beam," submitted to Laser Part. Beams.
[24]T. Antonsen and P. Mora, Phys. Rev. Lett. **69**, 2204 (1992).
[25]R. J. Mason and C. W. Cranfill, IEEE Trans. Plasma Sci. **PS-14**, 45 (1986).
[26]M. E. Glinsky, R. J. Mason, and M. Tabak, Bull. Am. Phys. Soc. **38**, 2080 (1993).
[27]G. B. Zimmerman and W. L. Kruer, Comments Plasma Phys. Controlled Fusion **2**, 85 (1975).
[28]See National Technical Information Service Document No. DE83002430 (D. S. Kershaw, "Computer simulation of suprathermal transport for laser fusion," in Laser Program Annual Report 80, UCRI-50021-80, pp. 3-78–3-83). Copies may be ordered from the National Technical Information Service, U.S. Department of Commerce, 5285 Port Royal Road, Springfield, Virginia 22161.
[29]M. D. Perry and G. Mourou, "Terawatt to Petawatt class subpicosecond Laser," to appear in Science.
[30]D. Strickland and G. Mourou, Opt. Commun. **56**, 219 (1985).